Front. Energy 2021, 15(4): 916–929
https://doi.org/10.1007/s11708-021-0757-9

RESEARCH ARTICLE

Chenglong WANG, Ran ZHANG, Kailun GUO, Dalin ZHANG, Wenxi TIAN, Suizheng QIU, Guanghui SU

Dynamic simulation of a space gas-cooled reactor power system with a closed Brayton cycle

Abstract Space nuclear reactor power (SNRP) using a gas-cooled reactor (GCR) and a closed Brayton cycle (CBC) is the ideal choice for future high-power space missions. To investigate the safety characteristics and develop the control strategies for gas-cooled SNRP, transient models for GCR, energy conversion unit, pipes, heat exchangers, pump and heat pipe radiator are established and a system analysis code is developed in this paper. Then, analyses of several operation conditions are performed using this code. In full-power steady-state operation, the core hot spot of 1293 K occurs near the upper part of the core. If 0.4 $ reactivity is introduced into the core, the maximum temperature that the fuel can reach is 2059 K, which is 914 K lower than the fuel melting point. The system finally has the ability to achieve a new steady-state with a higher reactor power. When the GCR is shut down in an emergency, the residual heat of the reactor can be removed through the conduction of the core and radiation heat transfer. The results indicate that the designed GCR is inherently safe owing to its negative reactivity feedback and passive decay heat removal. This paper may provide valuable references for safety design and analysis of the gas-cooled SNRP coupled with CBC.

Keywords gas-cooled space nuclear reactor power, closed Brayton cycle, system startup and shutdown, positive reactivity insertion accident

Received Aug. 28, 2020; accepted Mar. 10, 2021; online Jul. 25, 2021

Chenglong WANG, Ran ZHANG, Kailun GUO, Dalin ZHANG, Wenxi TIAN (✉), Suizheng QIU (✉), Guanghui SU

Department of Nuclear Science and Technology, State Key Laboratory of Multiphase Flow in Power Engineering, Shaanxi Key Laboratory of Advanced Nuclear Energy and Technology, Xi'an Jiaotong University, Xi'an 710049, China

E-mails: wxtian@mail.xjtu.edu.cn (Wenxi TIAN);
szqiu@mail.xjtu.edu.cn (Suizheng QIU)

Special Issue: Innovative Nuclear Energy Technology

1 Introduction

Space nuclear reactor power (SNRP) systems are especially suitable for space missions where the solar energy is nonexistent or instantaneous high-power is required. The technical route of developing SNRP must consider many factors. Regarding the complexity and weight of the system, space reactors are mainly fast neutron spectrum reactors to omit the neutron moderation system, at the cost of the low combustion rate of U^{235} [1]. Taking into account the technology maturity and the matching degree with energy conversion modes, the main cooling methods used in the space reactors are (sodium or lithium) heat pipe cooling, liquid metal (liquid sodium potassium alloy or lithium) cooling, and noble gas (helium and xenon gas mixture) cooling [2].

Heat pipe cooled reactor (HPCR) [3,4] has the advantages of simple system structure, single-point failure prevention, passive decay heat removal, and unnecessary special thawing. It mainly utilizes thermoelectric (TE) and Stirling cycle to produce electricity. However, due to the limitation of the heat transfer efficiency of the heat pipes, the HPCR is suitable for low power requirements of 1–100 kW_e. Liquid metal cooled reactor (LMCR) [5–7] features high heat transfer efficiency and small system pressure. The energy conversion technologies it uses mainly includes TE, thermionic fuel element (TFE), alkali metal thermal-to-electric conversion (AMTEC), and Stirling cycle. The LMCR can achieve electrical power output of hundred-kilowatt and its power scalability is better than that of HPCR. Unfortunately, the liquid metal loop is easy to freeze and it is difficult to restart after freezing. The thawing problem of the cooling system in the space environment must be considered. Gas cooled reactor (GCR) [8–10] can allow a very high core temperature, which enables the reactor to drive a closed Brayton cycle (CBC) or magneto-hydro-dynamic (MHD) for high-power electricity generation of more than 100 kW_e, especially for megawatt-class demand. Of course, there are still some key technical issues that need to be overcome about gas-cooled

SNRP. For example, the kinematic disturbances caused by moving turbomachinery must be avoided.

As a future development trend, high-power SNRP is irreplaceable for advanced nuclear electric propulsion (NEP). In view of the relatively low technological maturity of MHD [11], the GCR coupled with CBC is evaluated as the most suitable development route. In fact, GCR is the only reactor that has the capacity to operate in sustained operations at these high temperatures.

The space GCRs have been widely discussed in recent years. In general, the research focuses on five reactor core designs, including the pebble bed core, the plate-type fuel core, the cermet fuel core, the open-grid core, and the pin-block core. The application of the pebble bed reactor (PBR) concept to space reactors was first conceived by the US space nuclear thermal propulsion (SNTP) program for lightweight and compact nuclear rocket [12]. But this design was subsequently replaced by a higher-performance miniature reactor engine (MITEE), which used plate-type fuel elements. In 1993, El-Genk et al. proposed a unique PBR design for nuclear thermal propulsion (NTP), NEP, and bimodal applications [13]. Recently, Li et al. designed a hundred-kilowatt level space reactor IGCR-200 based on the research on high-temperature GCR of Tsinghua University. The IGCR-200 used integrated plate-fin fuel element based on the optimized TRISO particle [14]. The cermet (ceramic metallic) fuel, a metallic matrix containing ceramic particles, was developed by General Electric (GE) and Argonne National Laboratory (ANL) in the 1960s for the nuclear rocket program [15]. It could satisfy the needs of high-temperature resistance, high-strength, and assurance of complete fission product retention. With excellent performance, the cermet fuel attracted much interest in the application of space high-temperature GCRs [16–18]. In 2009, Russia proposed an open-grid space reactor core with a lighter mass for MW_e nuclear spacecraft, which drew much attention in the design of megawatt-class GCRs [9,19]. For pin-block core, the most mature research was the Prometheus Project established by National Aeronautics and Space Administration (NASA) in 2003 [8], whose goal was to develop the first NEP spaceship and demonstrate that it could be operated safely and reliably for deep-space exploration. Then, King et al. designed an innovative pin-block core submersion-subcritical safe space (S^4) reactor [20].

At present, the development of gas-cooled SNRP with CBC is in its infancy. Most of the work has been devoted to design and analysis of GCRs instead of integrated SNRP system [21–26]. The Prometheus Project conducted comprehensive work on the integrated gas-cooled SNRP thus a valuable database was available [8,27]. Based on the design of Prometheus, a system analysis code for gas-cooled SNRP is developed and verified in this paper. In addition, the transient thermal-hydraulic analyses of gas-cooled SNRP under different operation conditions are performed. In full-power steady-state operation, the core hot spot of 1293 K occurs near the upper part of the core. If 0.4 $ reactivity is introduced into the core, the maximum temperature that the fuel can reach is 2059 K, which is 914 K lower than the fuel melting point. The system finally has the ability to achieve a new steady-state with a higher reactor power. When the GCR is shut down in an emergency, the residual heat of the reactor can be removed through the conduction of the core and radiation heat transfer. The results indicate that the designed GCR is inherently safe owing to its negative reactivity feedback and passive decay heat removal. This paper may provide valuable references for safety design and analysis of the gas-cooled SNRP coupled with CBC.

2 System description and model development

Figure 1 presents the schematic diagram of the gas-cooled SNRP with CBC. The GCR serves as a heat source to heat the He-Xe working fluid. The Brayton loop converts the heat energy of the high-temperature gas into electricity. The system equips itself with a recuperator (RC) to improve the cycle efficiency. The heat rejection loop is connected to the Brayton loop via the gas cooler (GC). The radiator panel, consisting of carbon/carbon fins and water heat pipes, removes the waste heat of the system to the space environment by radiative heat transfer.

Figure 2 shows the cross-sectional views of the GCR and the flow path of the He-Xe gas in the reactor. The core consists of 313 fuel pins and one core block. There are 313 cylindrical holes with a diameter larger than the diameter of the fuel pin on the core block. The fuel pins are inserted into these holes. Then, an annular gas flow passage along each fuel pin between the outer surface of fuel pin and the surface of hole is defined (as shown in Fig. 2(b)). The fuel used in the GCR is 93.15% enriched uranium nitride (UN) that is clad with Re-lined Nb-Zr cladding, as demonstrated in Fig. 3. There is a gas gap between the fuel and the liner, which allows fission gas to flow into the gas plenum zone. Table 1 lists the major dimensions of the GCR for the SNRP [27].

2.1 Reactor model

Figure 4 illustrates the reactor model that couples the neutronics sub-model to the thermal-hydraulic sub-model. The GCR core presents a hexagonal layout with 10 rings of fuel pins around a central fuel pin. Then, the hexagonal layout is simplified and equivalent to a circular layout in the thermal-hydraulic model. According to the layout, the core block is divided into 11 cylinder regions, each containing one ring of fuel pins (as shown in Fig. 5(a)). The radial heat conduction among these cylinder block regions is also considered. Considering the symmetry, only one fuel pin in each ring is shown and modeled. The

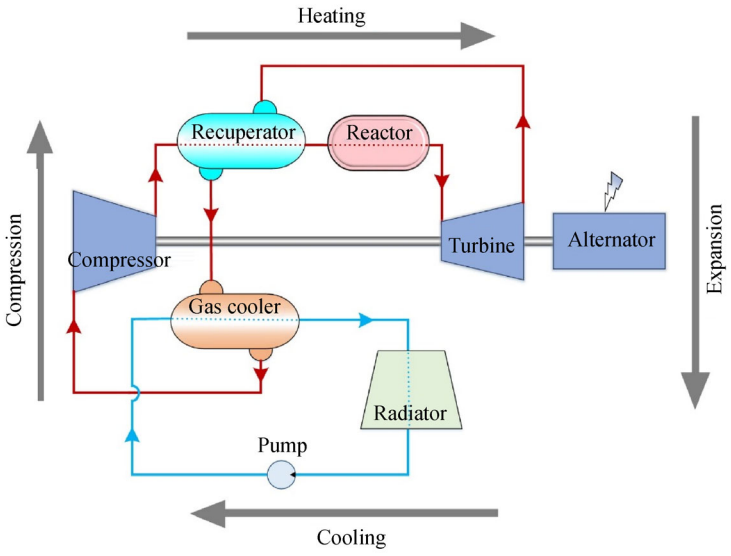

Fig. 1 A schematic diagram of a gas-cooled SNRP with a direct gas Brayton cycle.

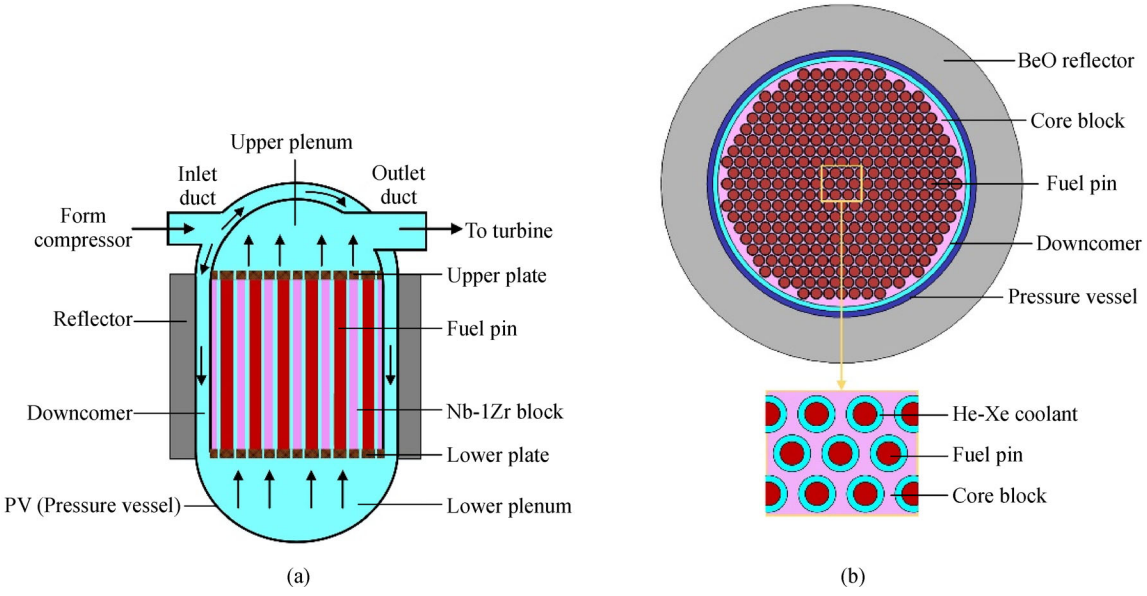

Fig. 2 Cross-sectional views of GCR.
(a) Axial view; (b) radial view.

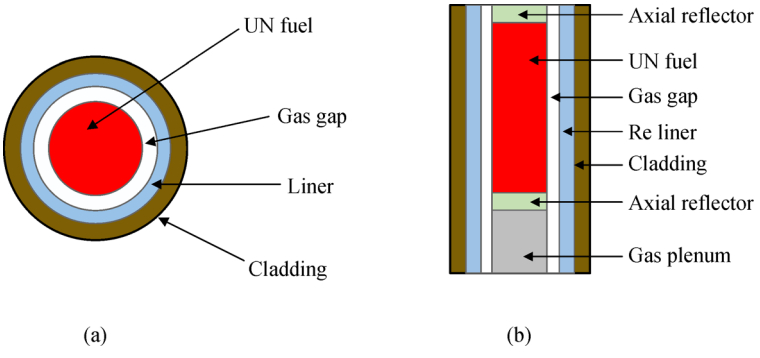

Fig. 3 Fuel pin of GCR.
(a) Radial view; (b) axial view.

reactor model includes 11 parallel flow passages, as shown in Fig. 5(b).

2.1.1 Reactor kinetics model

The six-group of precursors point kinetics equations, which assume that the profile of reactor power density do not change with time, are adopted to calculate the reactor fission power. Besides the fission power, the reactor decay power is also considered in this model. Although it occupies a very small proportion during normal operation, it is particularly important during shutdown transient. Four groups of fission products are used to calculate the decay power. These equations are listed in Eq. (1) through Eq. (4).

$$\frac{\mathrm{d}P_{\mathrm{fiss}}(t)}{\mathrm{d}t} = \frac{\rho(t)-\sum_{i=1}^{6}\beta_i}{\Lambda}P_{\mathrm{fiss}}(t)+\sum_{i=1}^{6}\lambda_i C_i(t), \quad (1)$$

$$\frac{\mathrm{d}C_i(t)}{\mathrm{d}t} = \frac{\beta_i}{\Lambda}P_{\mathrm{fiss}}(t)-\lambda_i C_i(t) \quad i=1,2,\ldots,6, \quad (2)$$

$$\frac{\mathrm{d}P_{\mathrm{decay},j}(t)}{\mathrm{d}t} = E_j P_{\mathrm{fiss}}(t)-\lambda_j P_{\mathrm{decay},j}(t) \quad j=1,2,3,4, \quad (3)$$

$$P_{\mathrm{eff}}(t) = \left(1-\sum_{j=1}^{4}E_j\right)P_{\mathrm{fiss}}(t)+\sum_{j=1}^{4}\lambda_j P_{\mathrm{decay},j}(t), \quad (4)$$

where P_{fiss} is the total fission power, λ_i is the decay constant for delayed neutron group i, β_i is the delayed neutron fraction for group i, C_i is the delayed neutron precursor concentration for group i, $P_{\mathrm{decay},j}$ is the decay power for fission product group j, λ_j is the decay constant for fission product group j, E_j is the effective energy fraction for fission product group j, and P_{eff} is the reactor effective power.

Furthermore, the kinetics model considers four reactivity feedback mechanisms. The total reactor reactivity can be expressed as

$$\rho(t) = \rho_{\mathrm{in}}(t)+\sum_{i=1}^{4}\alpha_i\left(T_{\mathrm{iavg}}(t)-T_{\mathrm{iref}}\right), \quad (5)$$

where ρ_{in} is the external inserted reactivity; α_i is the feedback coefficient that includes the fuel, core block,

Table 1 Design dimensions of GCR for SNRP system

Component	Dimension	Component	Dimension
Fuel enrichment	93.15%	Axial BeO reflector length	50 mm
Theoretical density	14.32 g/mL	Fuel pin pitch	15.5 mm
UN density	97.19%	Number of fuel pins	313
UN fuel diameter	10.0 mm	He gas mole fraction	63.5%
UN fuel height	450 mm	Core diameter	30.2 cm
Gas gap thickness	0.07 mm	Pressure vessel inner diameter	31.4 cm
Re liner thickness	0.7 mm	Pressure vessel outer diameter	32.8 cm
Nb-Zr cladding thickness	0.508 mm	Radial reflector inner diameter	33.0 cm
Coolant passage thickness	0.9 mm	Radial reflector outer diameter	55.0 cm
Gas plenum length	40 mm		

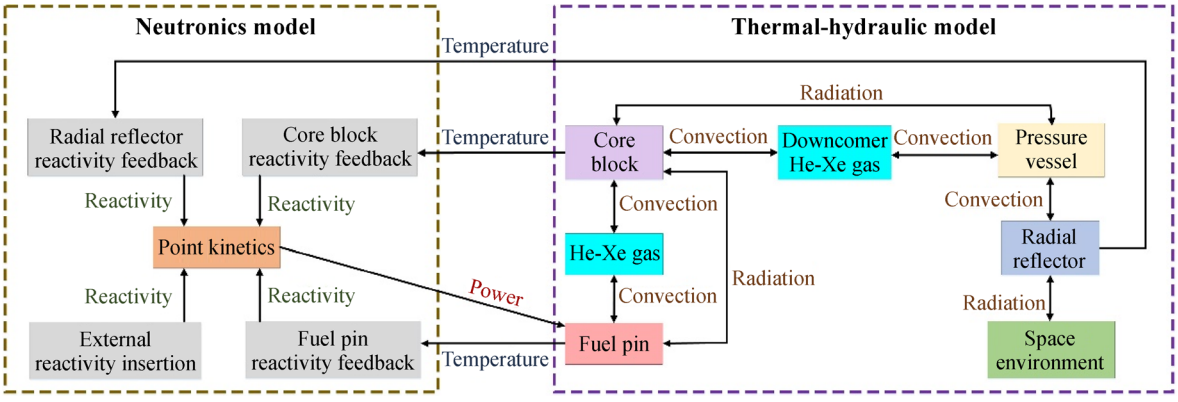

Fig. 4 Sub-models involved in reactor model.

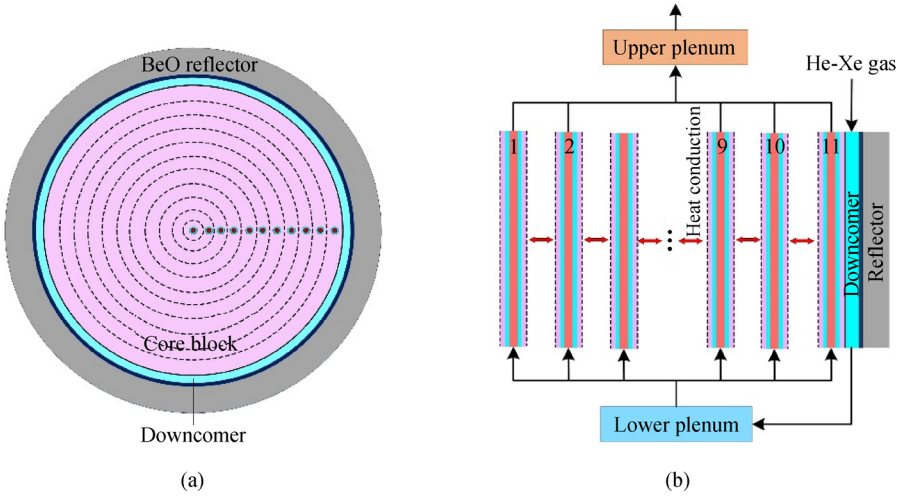

Fig. 5 Reactor thermal-hydraulic model.
(a) Radial view; (b) axial view.

pressure vessel (PV) and the coolant; T_{iavg} is the average temperature; and T_{iref} is the reference temperature.

2.1.2 Thermal-hydraulic model

The thermal-hydraulic model for the GCR consists of the fuel pin heat conduction, the gas heat convection, and the core block heat conduction, in addition to the downcomer flow region. The control volume division for one flow passage is depicted in Fig. 6.

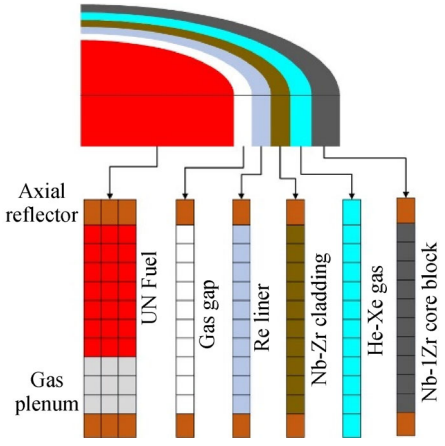

Fig. 6 Control volume division for one flow passage.

1) Solid heat conduction

The governing equations for all solids in the core are essentially the radial heat conduction equation.

$$\frac{\partial(\rho_{\mathrm{s}}c_{\mathrm{p,s}}T_{\mathrm{s}})}{\partial t}=\frac{1}{r}\frac{\partial}{\partial r}\left(rk_{\mathrm{s}}\frac{\partial T_{\mathrm{s}}}{\partial r}\right)+Q_{\mathrm{s}}, \tag{6}$$

where Q_{s} is the volumetric heat source. For the UN fuel, Q_{s} is calculated by the reactor power. For the gas plenum, gas gap, liner, cladding, PV, and reflector, Q_{s} is equal to zero. Especially for the xth ring core block, Q_{s} includes the radiative heat transfer with the outer surface of the fuel pin and heat convection with the gas coolant, given as

$$Q_{\mathrm{s}}=\frac{M_{\mathrm{f},x}\cdot 2\pi H_{\mathrm{b},x}}{V_{\mathrm{b},x}}[h_{\mathrm{gb}}(T_{\mathrm{g},x}-T_{\mathrm{b},x})R_{\mathrm{pout}}+\varepsilon_{\mathrm{fb}}\sigma(T_{\mathrm{fout},x}^4-T_{b,x}^4)R_{\mathrm{pin}}], \tag{7}$$

$$\varepsilon_{\mathrm{fb}}=\frac{1}{\frac{1}{\varepsilon_{\mathrm{fout}}}+\frac{S_{\mathrm{pin}}}{S_{\mathrm{pout}}}\left(\frac{1}{\varepsilon_{\mathrm{bin}}}-1\right)}, \tag{8}$$

where $M_{\mathrm{f},i}$ is the fuel pin number for xth block region, and $\varepsilon_{\mathrm{fout}}$ and $\varepsilon_{\mathrm{bin}}$ are the fuel pin and the core block emissivity, respectively.

Besides the convection heat transfer with He-Xe gas, there also exists the radiation heat transfer between the outer surface of the fuel pin and the core block. The boundary condition for the fuel pin:

$$k_{\mathrm{f}}\frac{\mathrm{d}T_{\mathrm{f}}}{\mathrm{d}r}\bigg|_{r=R_{f\,\mathrm{out}}}=h_{\mathrm{gf}}(T_{\mathrm{fout}}-T_{\mathrm{g}})+\varepsilon_{\mathrm{fb}}\sigma(T_{\mathrm{fout}}^4-T_{\mathrm{bin}}^4). \tag{9}$$

The outer surface of the core block:

$$k_{\mathrm{b}}\frac{\mathrm{d}T_{\mathrm{b}}}{\mathrm{d}r}\bigg|_{r=R_{\mathrm{bout}}}=h_{\mathrm{db}}(T_{\mathrm{bout}}-T_{\mathrm{d}})+\varepsilon_{\mathrm{bv}}\sigma(T_{\mathrm{bout}}^4-T_{\mathrm{pvin}}^4), \tag{10}$$

$$\varepsilon_{\mathrm{bv}}=\frac{1}{\frac{1}{\varepsilon_{\mathrm{bout}}}+\frac{S_{\mathrm{bout}}}{S_{\mathrm{pvin}}}\left(\frac{1}{\varepsilon_{\mathrm{pvin}}}-1\right)}. \tag{11}$$

The inner surface of the pressure vessel:

$$k_{\mathrm{pv}}\frac{\mathrm{d}T_{\mathrm{pv}}}{\mathrm{d}r}\bigg|_{r=R_{\mathrm{pvin}}} = h_{\mathrm{db}}(T_{\mathrm{d}}-T_{\mathrm{pvin}}) + \frac{S_{\mathrm{bout}}}{S_{\mathrm{pvin}}}\cdot\varepsilon_{\mathrm{bv}}\sigma(T_{\mathrm{bout}}^4-T_{\mathrm{pvin}}^4). \quad (12)$$

The radial reflector is cooled by space radiation:

$$k_{\mathrm{r}}\frac{\mathrm{d}T_{\mathrm{r}}}{\mathrm{d}r}\bigg|_{r=R_{\mathrm{rout}}} = \varepsilon_{\mathrm{rout}}\sigma(T_{\mathrm{rout}}^4-T_{\mathrm{sp}}^4), \quad (13)$$

where $\varepsilon_{\mathrm{rout}}$ is the emissivity of reflector, T_{rout} is the reflector outer surface temperature, and T_{sp} is the space environment temperature. The pipes of the system cooled by space radiation have the same form as those in Eq. (13).

2) He-Xe gas heat convection

In both the downcomer and the core, the He-Xe gas flows in the annular coolant channel. The gravity effect is negligible due to the space environment. The governing equations of the He-Xe gas flow can be expressed as

$$\frac{\partial\rho_{\mathrm{g}}}{\partial t}+\frac{\partial}{\partial z}\left(\frac{W_{\mathrm{p}}}{A_{\mathrm{p}}}\right)=0, \quad (14)$$

$$\frac{\partial}{\partial t}\left(\frac{W_{\mathrm{p}}}{A_{\mathrm{p}}}\right)+\frac{\partial}{\partial z}\left(\frac{W_{\mathrm{p}}^2}{\rho_{\mathrm{g}}A_{\mathrm{p}}^2}\right)=-\frac{\partial p_{\mathrm{p}}}{\partial z}-\frac{f_{\mathrm{p}}W_{\mathrm{p}}|W_{\mathrm{p}}|}{2D_{\mathrm{p}}\rho_{\mathrm{g}}A_{\mathrm{p}}^2}, \quad (15)$$

$$\frac{\partial(\rho_{\mathrm{g}}c_{p,\mathrm{g}}T_{\mathrm{g}})}{\partial t}+\frac{\partial}{\partial z}\left(\frac{W_{\mathrm{p}}c_{p,\mathrm{g}}T_{\mathrm{g}}}{A_{\mathrm{p}}}\right)=Q_{\mathrm{inner}}+Q_{\mathrm{outer}}, \quad (16)$$

where Q_{inner} and Q_{outer} are the heating power of inner wall and outer wall of the coolant passage, respectively. For the lower and upper plenums, Q_{inner} and Q_{outer} are equal to zero.

For the core:

$$Q_{\mathrm{inner}}=\frac{h_{\mathrm{gf}}\cdot 2\pi R_{\mathrm{pin}}(T_{\mathrm{fout}}-T_{\mathrm{g}})}{A_{\mathrm{p}}},$$

$$Q_{\mathrm{outer}}=\frac{h_{\mathrm{gb}}\cdot 2\pi R_{\mathrm{pout}}(T_{\mathrm{bin}}-T_{\mathrm{g}})}{A_{\mathrm{p}}}. \quad (17)$$

For the downcomer:

$$Q_{\mathrm{inner}}=\frac{h_{\mathrm{db}}\cdot 2\pi R_{\mathrm{din}}(T_{\mathrm{cb}}-T_{\mathrm{d}})}{A_{\mathrm{d}}}$$

$$Q_{\mathrm{outer}}=\frac{h_{\mathrm{dv}}\cdot 2\pi R_{\mathrm{dout}}(T_{\mathrm{pv}}-T_{\mathrm{d}})}{A_{\mathrm{d}}}, \quad (18)$$

where h_{gf} is the convective heat transfer coefficient between fuel pin and He-Xe gas, and h_{gb} is the convective heat transfer coefficient between He-Xe gas and core block. The convective heat transfer correlation is given as [28]

$$Nu=\frac{(\xi/8)RePr}{1.07+12.7\sqrt{(\xi/8)}(Pr^{2/3}-1)}\theta^{-0.505\lg\theta-0.165}, \quad (19)$$

$$\xi=(1.82\log Re-1.64)^{-2}, \quad (20)$$

where θ is the temperature ratio of the wall to the main fluid, reflecting the effects of property variation on the heat transfer performance.

2.2 Turbomachinery model

The turbine, alternator and compressor (TAC) are arranged in the same shaft, rotating at the same speed. The TAC shaft speed is determined by the power balance on the shaft, expressed as

$$P_{\mathrm{shaft}t}=P_{\mathrm{tur}}-P_{\mathrm{com}}-P_{\mathrm{alt}}, \quad (21)$$

$$P_{\mathrm{tur}}=W_{\mathrm{tur}}\cdot c_{p,\mathrm{g}}\cdot(T_{\mathrm{Tin}}-T_{\mathrm{Tout}}), \quad (22)$$

$$P_{\mathrm{com}}=W_{\mathrm{com}}\cdot c_{p,\mathrm{g}}\cdot(T_{\mathrm{Cout}}-T_{\mathrm{Cin}}), \quad (23)$$

$$\frac{\mathrm{d}N_{\mathrm{shaft}}}{\mathrm{d}t}=\frac{P_{\mathrm{shaft}}}{I\cdot N_{\mathrm{shaft}}\cdot 4\pi^2}, \quad (24)$$

where P_{shaft} is shaft power, P_{tur} is the power generated by the turbine, P_{com} is the power consumed by the compressor, P_{alt} is the power load on the alternator, N_{shaft} is shaft speed, and I is the moment of inertia.

The equations for the turbine and the compressor are essentially the characteristic curves that describe the shaft speed, flow rate, pressure ratio (Pr), and temperature ratio (Tr). The fine data for turbomachinery is provided by Wright et al. [27]. An additional important component for the SNRP is the power management and distribution subsystem (PMAD), which is responsible for regulating voltage and distributing power, as well as controlling shaft speed by adjusting the total electrical load on the alternator. The function of the PMAD is usually realized by a proportional, integral, differential (PID) controller, whose principle is illustrated in Fig. 7.

2.3 Recuperator model

The thermal-hydraulic model of recuperator discretizes the low-pressure side (LPS), high-pressure side (HPS), and intermediate heat transfer plate into small axial control volumes (as displayed in Fig. 8). The gas cooler model is not described here, since it is similar to the recuperator model. The structure parameters of the recuperator and the gas cooler are provided by Levine et al. [8]. The governing equations of this model are expressed as

Low-pressure side:

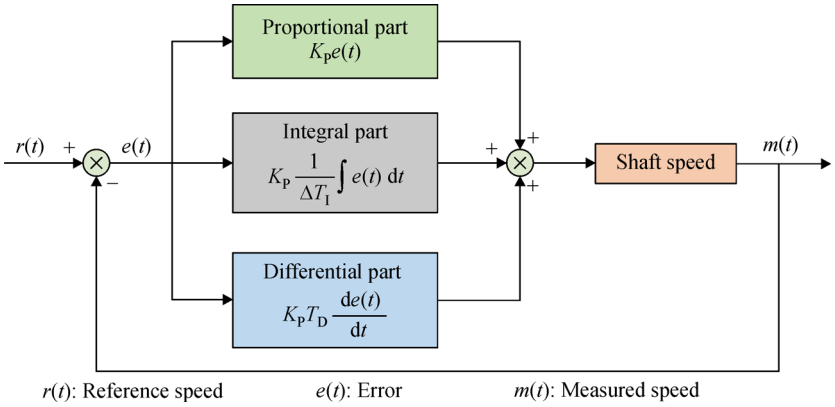

Fig. 7 Principle of PID speed controller.

$$\frac{\partial(\rho_{\mathrm{RCL}} c_{p,\mathrm{RCL}} T_{\mathrm{RCL}})}{\partial t} + \frac{\partial}{\partial z}\left(\frac{W_{\mathrm{RCL}} c_{p,\mathrm{RCL}} T_{\mathrm{RCL}}}{A_{\mathrm{RCL}}}\right) = \frac{h_{\mathrm{RCL}} \cdot \pi D_{\mathrm{RCP}} N_{\mathrm{RCP}} \cdot (T_{\mathrm{pw}} - T_{\mathrm{RCL}})}{A_{\mathrm{RCL}}}, \tag{25}$$

$$-k_{\mathrm{pw}} \frac{\mathrm{d}T_{\mathrm{pw}}}{\mathrm{d}r}\bigg|_{r=R_{\mathrm{pwL}}} = h_{\mathrm{RCL}} \cdot (T_{\mathrm{pw}} - T_{\mathrm{RCL}}), \tag{26}$$

High-pressure side:

$$\frac{\partial(\rho_{\mathrm{RCH}} c_{p,\mathrm{RCH}} T_{\mathrm{RCH}})}{\partial t} + \frac{\partial}{\partial z}\left(\frac{W_{\mathrm{RCH}} c_{p,\mathrm{RCH}} T_{\mathrm{RCH}}}{A_{\mathrm{RCH}}}\right) = \frac{h_{\mathrm{RCH}} \cdot \pi D_{\mathrm{RCP}} N_{\mathrm{RCP}} \cdot (T_{\mathrm{pw}} - T_{\mathrm{RCH}})}{A_{\mathrm{RCH}}}, \tag{27}$$

$$-k_{\mathrm{pw}} \frac{\mathrm{d}T_{\mathrm{pw}}}{\mathrm{d}r}\bigg|_{r=R_{\mathrm{pwH}}} = h_{\mathrm{RCH}} \cdot (T_{\mathrm{pw}} - T_{\mathrm{RCH}}), \tag{28}$$

Heat transfer plate:

$$\frac{\partial(\rho_{\mathrm{pw}} c_{p,\mathrm{pw}} T_{\mathrm{pw}})}{\partial t} = \frac{1}{r}\frac{\partial}{\partial r}\left(r k_{\mathrm{pw}} \frac{\partial T_{\mathrm{pw}}}{\partial r}\right). \tag{29}$$

2.4 Gas coolant mass model

The inventory of the He-Xe gas in the closed loop is fixed under transient conditions, thus the sum of the mass of the He-Xe gas within all components equals the initial fill mass. The absolute pressure of the system is determined by the gas coolant mass model as

$$\sum_n \frac{p_n \cdot V_n}{R_{\mathrm{g}} \cdot T_n} = m_{\mathrm{fill}}, \tag{30}$$

where V_n is the volume of different components, R_{g} is the gas constant, and m_{fill} is the initial fill mass of He-Xe gas.

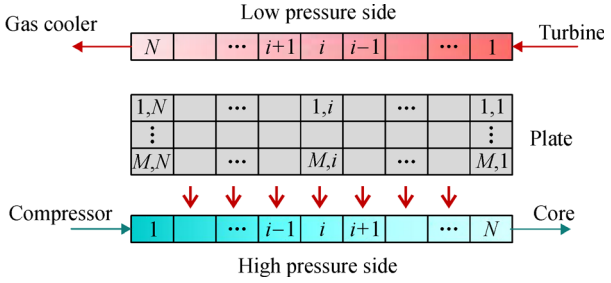

Fig. 8 Recuperator model.

3 Code development and verification

3.1 System analysis code development

First, all transient governing equations related to spatial coordinates are discretized using the control volume integration method to eliminate the derivative term of the spatial variable. Hereafter, all the governing equations can be unified into a coupled, nonlinear ordinary differential equations set, expressed as

$$\begin{aligned} y' &= f(y,t), \\ y_0 &= y(t_0), \end{aligned} \tag{31}$$

where parameters y can be the power, pressure, enthalpy, mass flow, shaft speed and so on, and y_0 is the initial values that adopt the design values [27] for the equations set.

Finally, the Gear method [29] that has a great advantage in solving stiff differential equations is employed to solve the equations set iteratively, and the time term is discretized by the backward difference method. The calculation result of each time step is outputted. When the convergence error is less than 10^{-6}, the calculation is considered to be stable.

The transient system code SAC-SPACE is completely self-developed using FORTRAN. To make SAC-SPACE easier to be updated and expanded, each component model

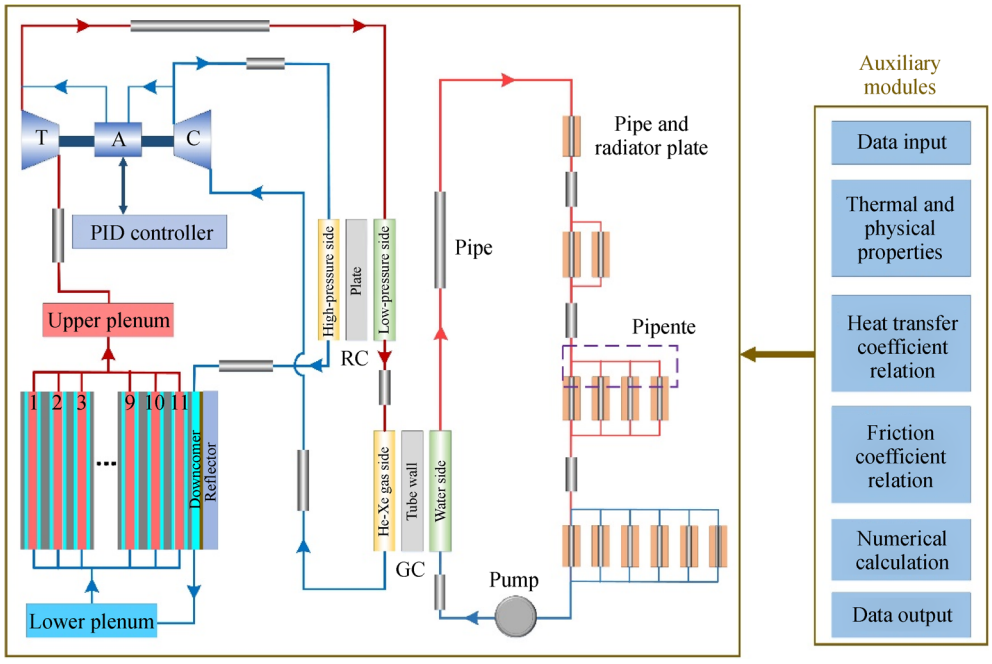

Fig. 9 Building blocks of SAC-SPACE for SNRPS.

is encapsulated into a module. Figure 9 shows the building blocks of SAC-SPACE for SNRPS.

3.2 System startup and code verification

Sandia National Laboratories developed a dynamic code RPCSIM to simulate the behavior of the SNRP system and fabricated a CBC test loop SBL-30 to validate the code [27]. The experimental data and modeled results are in good agreement. Under the same startup conditions, the startup initial for the gas-cooled SNRP is simulated by the SAC-SPACE, whose calculation results are compared with those of the RPCSIM to provide a verification for the SAC-SPACE. For the gas-cooled SNRP startup, the reactor is started first, followed by the CBC machinery. The system initial temperature is assumed to be 225 K. The SAC-SPACE is programmed to initiate the turbo-machinery when the average fuel temperature exceeds the initial temperature by 300 K. The system is filled with 2.49 kg of He-Xe gas, which corresponds to a system initial pressure of 0.7 MPa. The modeled results of the startup transient are illustrated in Figs. 10–14.

3.2.1 Phase 1: Zero power startup (0–1500 s)

At 0 s, an external reactivity of 0.12 $ is inserted into the core to start the reactor. Figures 10 and 11 plot the changes of reactor reactivity and power, respectively. The reactor power rises due to positive reactivity insertion until the fuel temperature grows large enough. At this time, the reactivity feedback effect would be important and

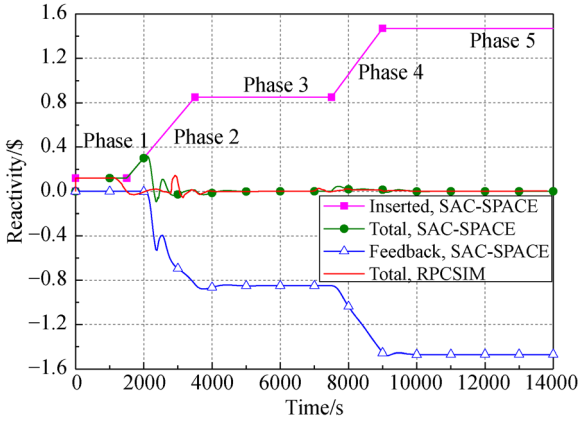

Fig. 10 Reactor reactivity in startup transient.

terminate the power increase, which leads to the first power peak. Obviously, the first power peak in the SAC-SPACE is later and larger than that in the RPCSIM (see Fig. 11). At 1500 s, the reactor power peaks at 18 kW in the RPCSIM but that only increases by 1.6 W in the SAC-SPACE. The reason for this difference is that the neutronics parameters applied in the two codes are different.

3.2.2 Phase 2: Reactivity insertion ramp (1500–3500 s)

In Phase 2, the reactivity is inserted into the core at a constant rate of 0.000365 $/s to sufficiently increase the fuel temperature so that the turbo-machinery can be

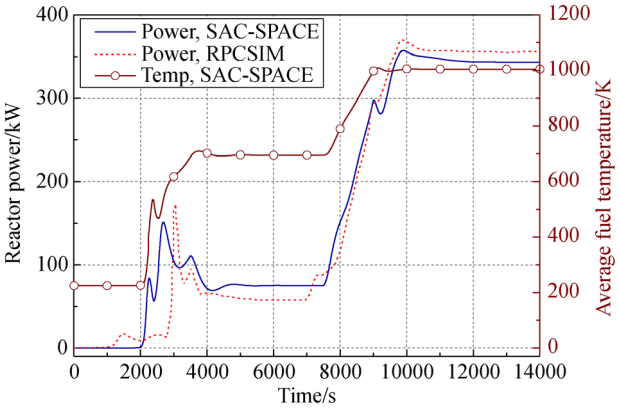

Fig. 11 Reactor power and average fuel temperature in startup transient.

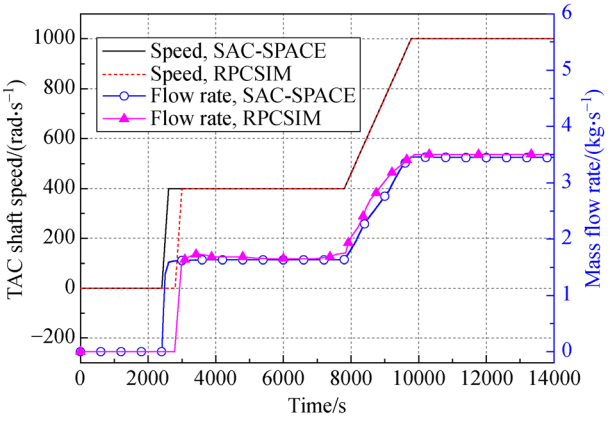

Fig. 12 TAC shaft speed and mass flow rate in startup transient.

started. The first power peak of the SAC-SPACE occurs at 2264 s with a value of 84 kW. At 2408 s, the average fuel temperature increases to the set point of 525 K. Figure 12 shows the variation of TAC shaft speed and mass flow rate. Once the preset point is reached, the PID controller starts the turbo-machinery and adjusts the TAC shaft speed to follow a prescribed curve. The shaft speed increases from 0 rad/s to 400 rad/s in 200 s. As a result, the mass flow rate of the system rises from 0 kg/s to 1.63 kg/s.

The flow pushes the He-Xe gas into the reactor, which decreases the core temperature (Fig. 11). Further, the fuel reactivity feedback and reactor power increase until the fuel temperature increases again. At 2686 s, the reactor power peaks at 151 kW. Compared with the SAC-SPACE, the CBC starts at 2800 s and the reactor power spikes to 180 kW at 3000 s in the RPCSIM. After this power peak, another smaller power spike is observed at 3500 s, which is caused by the suddenly decreased reactivity insertion slope.

3.2.3 Phase 3: Low power steady-state (3500–7500 s)

In Phase 3, the external reactivity is kept at 0.85 $ and the shaft speed is held at 400 rad/s. There is enough time to allow the system to achieve steady-state. The power is 75 kW, about 19% of the design value of 400 kW. The maximum fuel temperature is 736 K that has a sufficient safety margin from the melting point. Therefore, this phase is a good stage to inspect the spacecraft system and ensure that the system can operate normally.

3.2.4 Phase 4: Transition to full power (7500–9780 s)

At the beginning of Phase 4, the inserted reactivity increases from 0.85 $ to 1.47 $ in 1500 s. The shaft speed starts to increase at 7800 s and reaches 1000 rad/s (full design speed) at 9780 s. Figures 13 and 14 illustrate the system temperatures and pressures, respectively. Increased temperature would cause internal pressurization as the inventory of the He-Xe gas in the system does not

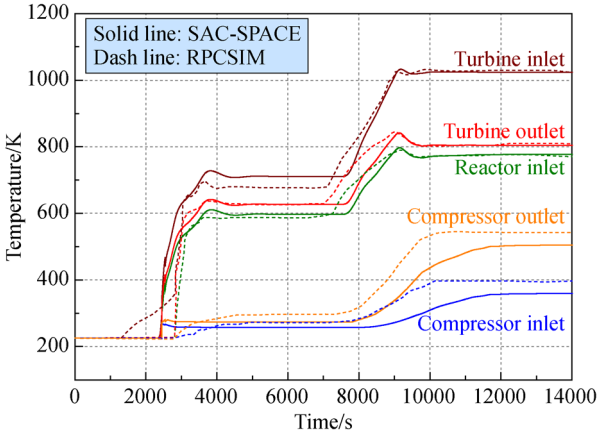

Fig. 13 System temperatures during the startup transient.

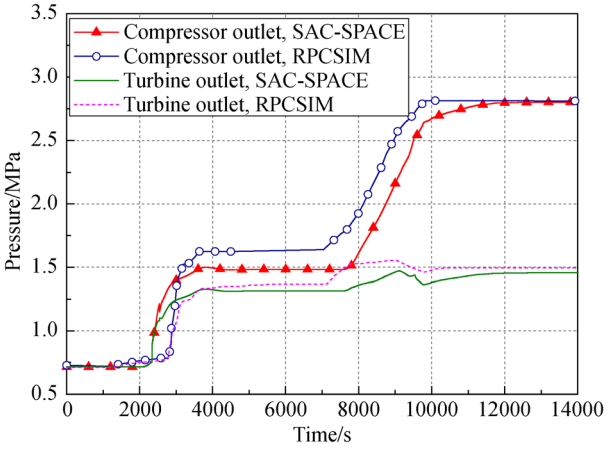

Fig. 14 System pressure during the startup transient.

change. Therefore, the transient responses of temperature and the pressure behave consistently. The system parameters show a relatively smooth increase in Phase 4.

3.2.5 Phase 5: Full power steady-state (9780–14000 s)

In Phase 5, both the external reactivity and the shaft speed are kept constant. After a while, the system achieves its steady-state with a reactor power of 344 kW (358 kW in the RPCSIM). The reactor outlet temperature reaches 1024 K (1026 K in the RPCSIM), which does not achieve the design value of 1150 K. The system mass flow rate is 3.45 kg/s which is slightly smaller than 3.50 kg/s calculated by the RPCSIM.

As a conclusion, the calculation results between SAC-SPACE and RPCSIM are in good agreement. The maximum deviation occurs at the initial stage of the reactor power increase, but it has little effect on the overall performance evaluation of the system.

4 Results and discussion

4.1 Steady-state analysis

Steady-state analysis is conducted to investigate the operation performance of the gas-cooled SNRP system. Table 2 lists the steady-state operation parameters of the system. Figure 15 shows the fuel temperature contour of the GCR core. The inner core region has a relatively high temperature. The maximum temperature (1293 K) occurs at the first core region. Figure 16 plots the axial temperature profiles of fuel zone in the first region. It can be seen that there is a considerable temperature reduction

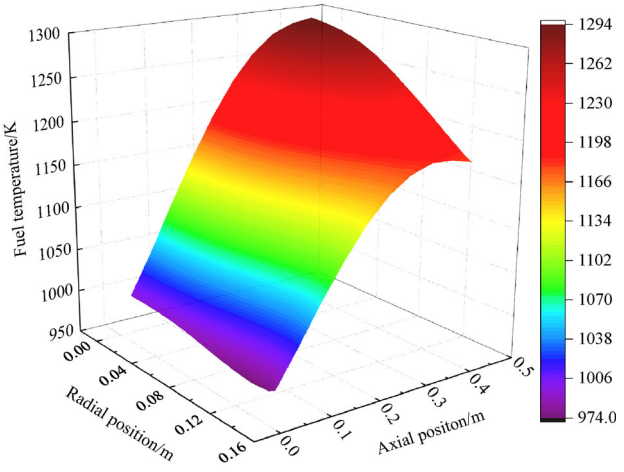

Fig. 15 Fuel temperature contour of GCR core.

in the gas gap due to its low heat conductivity. The steady-state calculation results are utilized as initial conditions for the transient calculation that follows.

4.2 Positive reactivity insertion accident

Accidental reactivity addition due to some faulty action of the control system would lead to a reactor power surge, endangering the safety of the fuel pin. In this section, it is assumed that an external reactivity of 0.4 $ is introduced into the reactor at 0 s without adopting any protection measures to demonstrate the dynamic response of the SNRP in the positive reactivity insertion accident (PRIA).

Figures 17 to 19 show the transient responses of the reactor in the PRIA. It can be observed that the positive reactivity addition causes the reactor power to rise sharply

Table 2 Steady-state parameters of the GCR SNRPS

Parameter	Value	Parameter	Value
Reactor inlet temperature/K	854	Compressor outlet pressure/MPa	2.999
Reactor outlet temperature/K	1153	RC HPS outlet temperature/K	854
Reactor inlet pressure/MPa	2.992	RC HPS inlet pressure/MPa	2.998
Reactor outlet pressure/MPa	2.958	RC HPS outlet pressure/MPa	2.993
Turbine outlet temperature/K	915	Radiator inlet temperature/K	463
Turbine inlet pressure/MPa	2.956	Radiator outlet temperature/K	345
Turbine outlet pressure/MPa	1.513	Radiator inlet pressure/MPa	7.744
RC LPS outlet temperature/K	568	Radiator outlet pressure/MPa	7.742
RC LPS inlet pressure/MPa	1.510	Mass flow rate/(kg·s^{-1})	3.1
RC LPS outlet pressure/MPa	1.508	Reactor power/kW$_t$	400
GC gas-side outlet temperature/K	362	Turbine power/kW$_t$	304
GC gas-side inlet pressure/MPa	1.507	Compressor power/kW$_t$	185
GC gas-side outlet pressure/MPa	1.500	Alternator power/kWt	119
Compressor outlet temperature/K	507	Conversion efficiency	29.8%
Compressor inlet pressure/MPa	1.499		

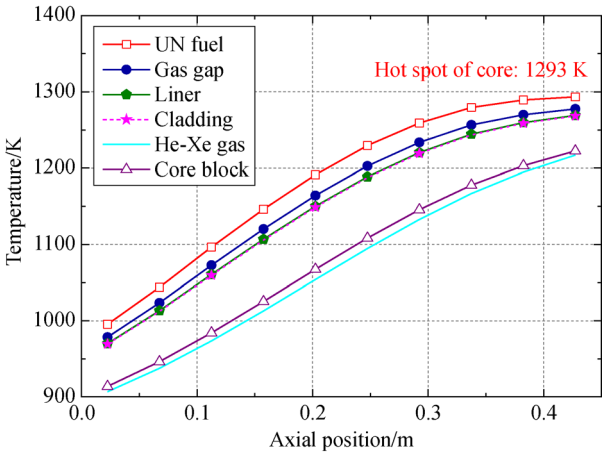

Fig. 16 Axial temperature profiles of fuel zone in first core region.

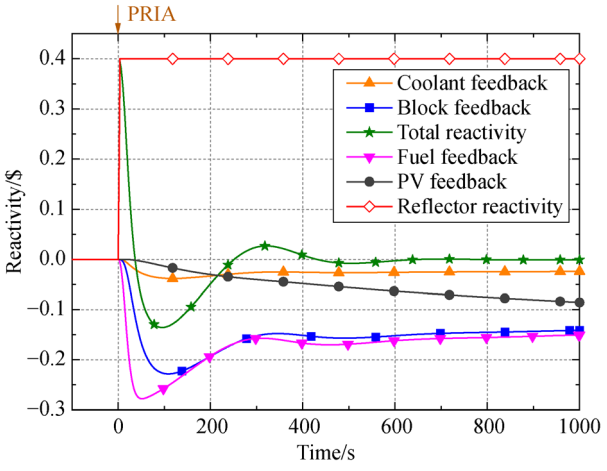

Fig. 17 Reactor reactivity in PRIA.

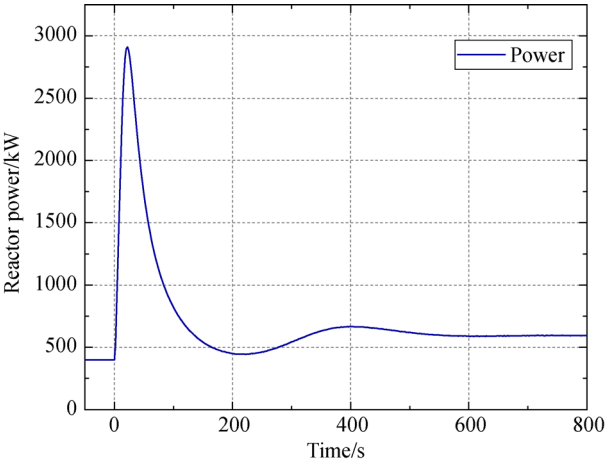

Fig. 18 Reactor power in PRIA.

within 22 s. Owing to the increased core temperature, the negative reactivity feedbacks restrain the power from

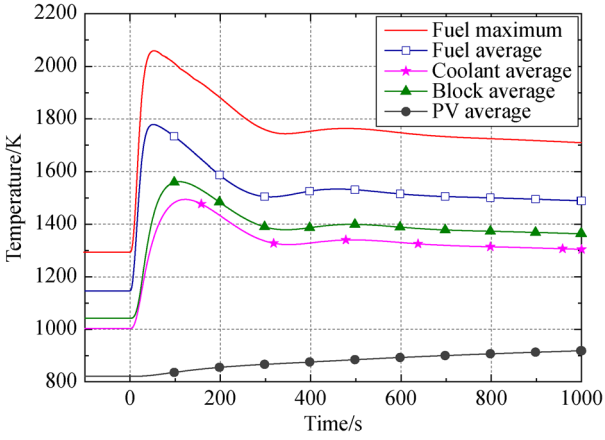

Fig. 19 Core temperatures during PRIA.

increasing. Soon after, the fuel and core block temperatures that are closely related to the power start to decrease. Unlike the fuel and block, the PV and radial reflector temperatures keep increasing. Finally, the reactor attains a new steady-state with a power of 569 kW_t. Meanwhile, the core temperature reaches a maximum of 2059 K, having a safety margin of 914 K from the fuel melting point.

The mass flow variation of the Brayton loop is plotted in Fig. 20. The turbine pressure ratio and TAC shaft speed determine the mass flow. Figure 21 displays the transient responses of the TAC power. The increase of the reactor power and the outlet temperature is large enough that the turbine power increases from 304 kW_t to 400 kW_t. The compressor power also rises, but by a smaller amount. The result is an increase in the alternator power in order to keep the shaft speed constant. If there is no adequate alternator load to be supplied, the shaft speed will increase until the TAC powers re-balance.

4.3 System shutdown transient

An important issue about space reactors is the safe removal

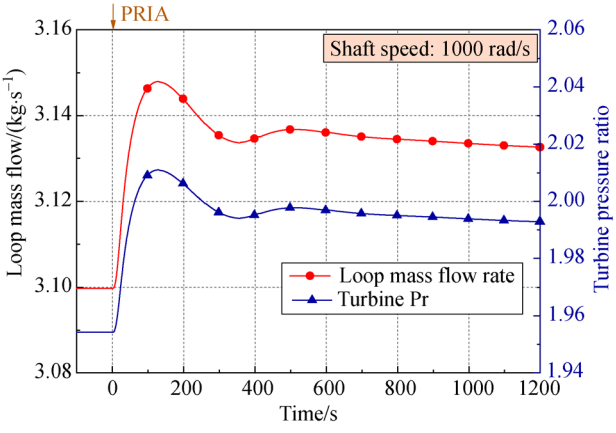

Fig. 20 Brayton loop flow rate and turbine pressure ratio in PRIA.

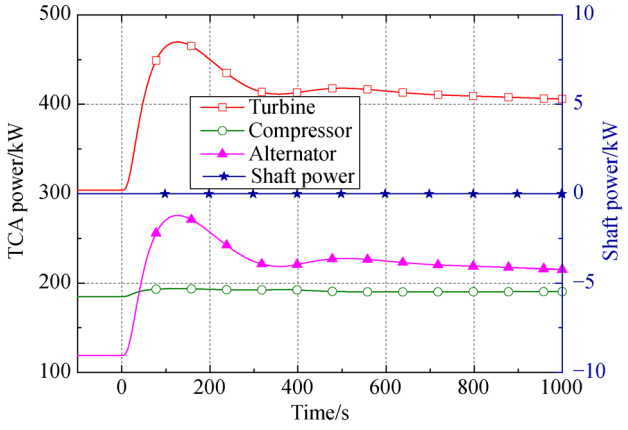

Fig. 21 Brayton component powers in PRIA.

of the decay heat after the system is shut down. There is no gravity in space, and the thermal conductivity of gas coolant is low. The analysis using only passive decay heat removal is performed first to investigate whether the reactor decay heat can be safely removed. In reality, it is impossible for the Brayton mechanical components to stop rotating immediately when the normal system shuts down. But if the Brayton TAC shaft fails, the system would be shut down in an emergency due to a sudden flow stop. This case models the most severe shutdown condition where the loop mass flow is reduced to zero within a short time. Once the reactor losses its coolant flow, the heat produced in the fuel would be transferred to the radial reflector via conduction through the core and radiative heat transfer in the gas coolant passage. Then the heat is removed to the space by the radiation of the radial reflector.

The reactor shutdown is initiated by inserting a negative reactivity of –7.0 $ at 0 s. Figure 22 shows the changes in the reactor power and reactivity in the shutdown transient. Note that the reactor fission power sharply decreases from 374 kW to 12 kW within 10 s, but the decay power reduces only by 4 kW to 21 kW. At about 6 s, the contribution of

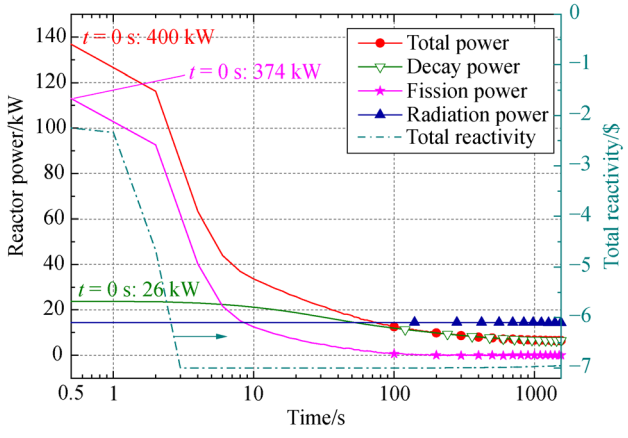

Fig. 22 Reactivity and reactor power in shutdown.

decay power to total power exceeds that of the fission power. The fission power is almost declined to 0 kW at 176 s. The radiation power gradually decreases as the core temperatures drop. The reactor temperatures are shown in Fig. 23. It can be observed that the core temperatures keep reducing in the shutdown transient.

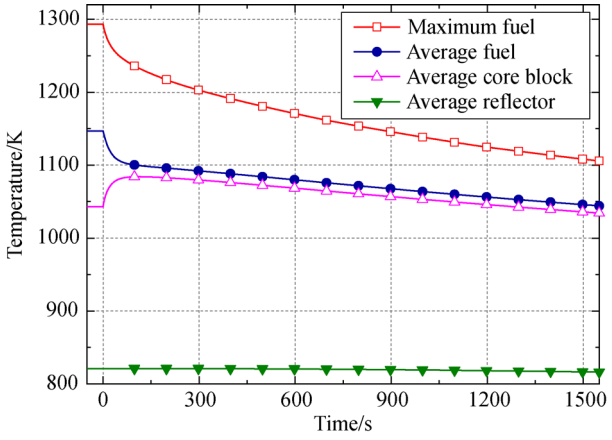

Fig. 23 Reactor temperatures in shutdown.

5 Conclusions

A transient system analysis code (SAC-SPACE) for the gas-cooled SNRP with CBC is developed to investigate the safety characteristics of the integrated system under different operation conditions. The main conclusions are summarized as follows:

The startup of the gas-cooled SNRP system is initiated by starting the GCR first and takes about 4 h to complete. The calculation results of the SAC-SPACE are in good agreement with those of the validated RPCSIM code, suggesting that the models of the SAC-SPACE are reasonable and accurate to simulate the dynamic behavior of the SNRP.

At full-power steady-state operation, the maximum fuel temperature of 1293 K is 1680 K lower than the fuel melting point, which provides a sufficient safe margin for the reactor in the event of an accident.

When the 0.4 $ reactivity is inserted into the core, the reactor power surges and stabilizes at 569 kW_t. The maximum fuel temperature is 2059 K with a safety margin of 914 K in the PRIA. At the new steady-state, the alternator power increases from 119 kW_t to 209 kW_t for the constant shaft speed. The system mass flow rate does not change much. This indicates that the SNRP system is capable of withstanding certain PRIAs through negative reactivity feedback of the GCR.

During the shutdown process, passive decay heat removal is sufficient to keep the core temperature down. This illustrates that the GCR described in this paper is inherently safe. However, this does not mean that all the space GCRs can be shut down safely by only relaying on

passive decay heat removal. For some GCRs, a period of active cooling (coolant flow) is required to cool the reactor at the start of shutdown. If necessary, a special auxiliary cooling system can be designed for the space GCRs shutdown.

Acknowledgements This work was supported by the National Natural Science Foundation of China (Grant No. U1967203), the National Key R&D Program of China (Grant No. 2019YFB1901100) and China Postdoctoral Science Foundation (Grant No. 2019M3737).

Notations

A	Flow area/m^2
C	Delayed neutron precursor concentration/m^{-3}
c_p	Specific heat capacity/$(J\cdot kg^{-1}\cdot K^{-1})$
D	Hydraulic diameter/m
E	Effective energy fraction
f	Friction coefficient
H	Height/m
h	Heat transfer coefficient/$(W\cdot m^{-2}\cdot K^{-1})$
I	Moment of inertia/$(kg\cdot m^2)$
k	Thermal conductivity $(W\cdot m^{-1}\cdot K^{-1})$
m	Mass/kg
M	Number
N	Shaft speed $(rad\cdot s^{-1})$
Nu	Nusselt number
P	Power/W
Pr	Prandtl number
p	Pressure/Pa
Q	Volumetric heat generation/$(W\cdot m^{-3})$
R	Radius/m
R_g	Gas constant/$(J\cdot kg^{-1}\cdot K^{-1})$
Re	Reynolds number
r	Radial coordinate/m
S	Area/m^2
T	Temperature/K
t	Time/s
V	Volume/m^3
W	Mass flow rate/$(kg\cdot s^{-1})$
z	Axial coordinate/m
ρ	Reactivity $(\Delta k\cdot k^{-1})$; Density/$(kg\cdot m^{-3})$
λ	Decay constant/s^{-1}
Λ	Neutron generation time/s
β	Delayed neutron fraction
ε	Emissivity
α	Reactivity feedback coefficient/$(\Delta k\cdot k^{-1}\cdot K^{-1})$
σ	Stefan-Boltzmann constant/$(5.67\times10^{-8}\ W\cdot m^{-2}\cdot K^{-4})$

Subscripts

alt	Alternator
b	Core block
bin	Core block inner surface
bout	Core block outer surface
bv	Core block and pressure vessel
com	Compressor
Cin	Compressor inlet
Cout	Compressor outlet
d	Downcomer
db	Downcomer and core block
decay	Decay
din	Downcomer inner
dout	Downcomer outer
dv	Downcomer and pressure vessel
eff	Effective
f	Fuel pin
fb	Fuel pin and core block
fiss	Fission
fout	Fuel pin outer surface
g	He-Xe gas
gb	Gas and core block
gf	Gas and fuel pin
i	delayed neutron group
iavg	Average
in	External reactivity
inner	Inner surface
iref	Reference
j	Fission product group
n	Component
outer	Outer surface
p	Annular gas passage
pin	Gas passage inner
pout	Gas passage outer
pv	Pressure vessel
pvin	Pressure vessel inner surface
pw	Plate wall
pwH	Plate wall high-pressure side
pwL	Plate wall low-pressure side
r	Radial reflector
rout	Radial reflector outer surface
RCH	Recuperator high-pressure side
RCL	Recuperator low-pressure side
RCP	Recuperator passage
s	Solid
shaft	TAC shaft

sp	Space environment
Tin	Turbine inlet
Tout	Turbine outlet
tur	Turbine
x	Core block ring

References

1. Wu W R, Liu J Z, Zhao X, et al. System engineering research and application foreground of space nuclear reactor power generators. Scientia Sinica Technologica, 2019, 49(1): 1–12 (in Chinese)
2. Akimov V N, Koroteev A A, Koroteev A S. Space nuclear power systems: yesterday, today, and tomorrow. Thermal Engineering, 2012, 59(13): 953–959
3. Poston D I. The heat pipe-operated mars exploration reactor (HOMER). In: AIP Conference Proceedings 2001. American Institute of Physics, 2001, 552: 797–804
4. Gibson M A, Poston D I, McClure P R, et al. Heat transport and power conversion of the Kilopower reactor test. Nuclear Technology, 2020, 206(sup1): 31–42
5. Staub D W. SNAP reactor programs: summary report. INIS Report AI-AEC-13067, 1973
6. Demuth S F. SP100 space reactor design. Progress in Nuclear Energy, 2003, 42(3): 323–359
7. Voss S S. TOPAZ-II design evolution. In: AIP Conference Proceedings 1994. American Institute of Physics, 1994, 301: 791–802
8. Levine B L. Space nuclear power plant pre-conceptual design report, for information. INIS Report SPP-67210–0010, 2006
9. Dragunov Y G. Fast-neutron gas-cooled reactor for the megawatt-class space bimodal nuclear thermal system. Engineering and Automation Problems, 2015, 2: 117–120 (in Russian)
10. Hu G, Zhao S Z. Overview of space nuclear reactor power technology. Journal of Deep Space Exploration, 2017, 4(5): 430–443 (in Chinese)
11. Li Y W, Zhang B L, Li Y H, et al. Applications and prospects of magnetohydrodynamics in aeronautical engineering. Advances in Mechanics, 2017, 47: 452–502 (in Chinese)
12. Ludewig H, Powell J R, Todosow M, et al. Design of particle bed reactors for the space nuclear thermal propulsion program. Progress in Nuclear Energy, 1996, 30(1): 1–65
13. El-Genk M S, Morley N J, Pelaccio D G, et al. Pellet bed reactor concepts for nuclear propulsion applications. Journal of Propulsion and Power, 1994, 10(6): 817–827
14. Li Z G, Sun J, Liu M L, et al. Design of a hundred-kilowatt level integrated gas-cooled space nuclear reactor for deep space application. Nuclear Engineering and Design, 2020, 361: 110569
15. Stewart M E M, Schnitzler B G. Thermal, fluid, and structural analysis of a cermet fuel element. In: Proceedings of the 48th AIAA/ASME/SAE/ASEE Joint Propulsion Conference & Exhibit, Atlanta, Georgia, USA, 2012
16. Kruger G B, Lobach J. Application of cermet fueled reactors to multimegawatt space power systems. In: Proceedings of the 24th Intersociety Energy Conversion Engineering Conference, Washington, USA, 1989: 1125–1130
17. Webb J A, Gross B J. A conceptual multi-megawatt system based on a tungsten cermet reactor. In: Proceedings of Nuclear and Emerging Technologies for Space 2011, Albuquerque, NM, USA, 2011: INL/CON-10–20348
18. Jahshan S N, Kammash T. Multimegawatt nuclear reactor design for plasma propulsion systems. Journal of Propulsion and Power, 2005, 21(3): 385–391
19. Meng T, Zhao F L, Cheng K, et al. Neutronics analysis of megawatt-class gas-cooled space nuclear reactor design. Journal of Nuclear Science and Technology, 2019, 56(12): 1120–1129
20. King J C, El-Genk M S. Submersion-Subcritical Safe Space (S^4) reactor. Nuclear Engineering and Design, 2006, 236(17): 1759–1777
21. Morley N J, El-Genk M S. Neutronics and thermal-hydraulics analyses of the pellet bed reactor for nuclear thermal propulsion. Nuclear Technology, 1995, 109(1): 87–107
22. Zhang R, Liang Y, Liu X, et al. Thermal-hydraulic analysis of pellet bed reactor for space nuclear electric propulsion. Annals of Nuclear Energy, 2020, 143: 107482
23. King J C, El-Genk M S. Thermal-hydraulic and neutronic analyses of the submersion-subcritical, safe space (S^4) reactor. Nuclear Engineering and Design, 2009, 239(12): 2809–2819
24. Schillo K J, Kumar A, Harris K E, et al. Neutronics and thermal hydraulics analysis of a low-enriched uranium cermet fuel core for a Mars surface power reactor. Annals of Nuclear Energy, 2016, 96: 307–312
25. El-Genk M S, Tournier J P, Gallo B M. Dynamic simulation of a space reactor system with closed Brayton cycle loops. Journal of Propulsion and Power, 2010, 26(3): 394–406
26. Zhang R, Guo K L, Wang C L, et al. Thermal-hydraulic analysis of gas-cooled space nuclear reactor power system with closed Brayton cycle. International Journal of Energy Research, 2020, online, https://doi.org/10.1002/er.5329
27. Wright S A, Lipinski R J, Vernon M E, et al. Closed Brayton cycle power conversion systems for nuclear reactors: modeling, operations, and validation. New Mexico: Sandia National Laboratories, 2006
28. Qin H, Zhang R, Guo K L, et al. Thermal-hydraulic analysis of an open-grid megawatt gas-cooled space nuclear reactor core. International Journal of Energy Research, 2020, online, https://doi.org/10.1002/er.5329 doi:10.1002/er.5329
29. Gear C W. Numerical Initial Value Problems in Ordinary Differential Equations. Englewood Cliffs, NJ: Prentice-Hall, 1971